Composites Science and Technology 201 (2021) 108541

Contents lists available at ScienceDirect

Composites Science and Technology

journal homepage: http://www.elsevier.com/locate/compscitech

# Laser induced graphene for in situ damage sensing in aramid fiber reinforced composites

LoriAnne Groo [a], Jalal Nasser [a], Daniel Inman [a], Henry Sodano [a,b,*]

[a] Department of Aerospace Engineering, University of Michigan, Ann Arbor, MI, 48109, United States
[b] Department of Materials Science and Engineering, University of Michigan, Ann Arbor, MI, 48109, United States

A B S T R A C T

In situ monitoring of strain and damage in fiber-reinforced composites provides critical information regarding the state of the material without requiring the structure to be removed from operation. In order to avoid the use of complex, heavy, and bulky sensor networks to track the state of the structure, recent focus has turned to multifunctional materials with inherent characteristics which enable in situ monitoring. This work investigates laser induced graphene (LIG) integrated within aramid fiber reinforced composites for damage and strain sensing during mechanical loading. The LIG used here fully integrates the sensing material within the composite as the piezoresistive graphene layer is coated directly onto the reinforcing aramid fabric prior to infusing the fibers with the supporting matrix. The sensing element is thus not susceptible to environmental effects and adds no extra weight while also maintaining the specific strength of the material. As strain and damage occur within the composite, the LIG proves capable of tracking strain and detecting plastic deformation in situ. Thus, the result of this work is the integration of a multifunctional component into aramid composites which possesses in situ sensing capabilities. Furthermore, the processes and materials are easily scalable for the large-scale production of multifunctional aramid fiber reinforced composites.

## 1. Introduction

With the rapidly expanding use of aramid fibers and aramid fiber reinforced composites, increasing attention has been placed on the structural health monitoring of such materials while in service. In situ monitoring is particularly beneficial in cyclic or unpredictable loading environments such as are experienced in aerospace and military applications, which are two of the key industries that take advantage of the light weight and impact damage resilience of aramid fibers [1]. In cases such as these, the loading environment can cause quickly propagating damage which can lead to complete failure of components or structures. Since current methods of inspecting the damage state of fiber reinforced composites typically require the structure under investigation to be temporarily removed from service for inspection, research involving in situ techniques for structural health monitoring and non-destructive damage detection has rapidly expanded. Currently, the majority of in situ damage detection methods require either the use of external sensors or the embedding of discrete fibers or sensors, however these add bulk or weight when included externally and increase the potential for delamination when embedded [2–5]. To overcome these obstacles, additional focus has been placed on in situ strain and damage sensing via multifunctional materials. By introducing additional functionality to the structure itself, the need for supplementary sensing systems is reduced or eliminated, thus lowering the demand on precious weight and space requirements. Among the wide variety of in situ sensing and structural health monitoring approaches, resistance-based sensing has been heavily investigated due to the simplicity of the approach and the ability to simultaneously sense and track both strain and damage.

Initially limited to conductive fiber reinforcement, such as carbon, the resistance-based sensing method relies on the detection of strain or damage via changes in the electrical conductivity of the composite [6–11]. Typically, a current is applied to the structure under investigation while the resulting voltage is concurrently measured, thus allowing for the calculation of the resistance using Ohm's law. As the carbon fiber-based composites are strained, the resistivity shows an increasing trend due to the stretching of the electrically conductive fibers [6]. Additionally, damage to the composite results in a sudden increase in the resistance of the composite due to alterations to the conductive fiber-fiber contacts, such as during fiber fracture or delamination [6]. Using the described methodology, the detection of both tensile strain and damage [6–8] as well as flexural strain and damage [9] via electrical resistance measurements has been investigated and demonstrated for carbon fiber composites. Furthermore, damage due to impact has also been determined deemed to be clearly detectable using one or more resistance measurements in carbon fiber-based composite plates [10]. However, the methodology used in the cited work is limited to

* Corresponding author. Department of Aerospace Engineering, University of Michigan, Ann Arbor, MI, 48109, United States.
*E-mail address:* hsodano@umich.edu (H. Sodano).

https://doi.org/10.1016/j.compscitech.2020.108541
Received 15 April 2020; Received in revised form 18 September 2020; Accepted 31 October 2020
Available online 4 November 2020

composites that employ conductive fiber reinforcement.

To expand the application of resistance-based strain and damage detection to include non-conductive fiber reinforced composites, such as glass or aramid fibers, later research has investigated the addition of conductive nanofillers such as carbon black, carbon nanotubes (CNTs), or graphene oxide [12–18]. Among these nanofillers, CNTs have received significant attention due to their beneficial structural properties when embedded within fiber-reinforced composites [19–23]. Additionally, CNTs also add piezoresistivity by forming electrically conductive pathways through the composite which are then altered or damaged during changing state, such as strain or damage to the material [12–15,17]. Glass fiber reinforced composites with embedded CNTs have been shown to be capable of sensing similar strain and damage patterns as conductive carbon fiber composites, namely under tensile [13], flexural [14], and impact [24] loading conditions; however, the majority of research has focused on the addition of CNTs to glass fiber-reinforced composites with less work completed on aramid fiber reinforced composites. This is due to the incompatibility of traditional CNT processing techniques with insulating polymer fibers, such as aramids, as the high temperature and harsh chemical environment necessary for chemical vapor deposition (CVD) weakens the fiber, while other benign methods such as electrophoretic deposition (EPD) require electrically conductive fibers [25–28].

Efforts to sidestep these issues by adding CNTs directly to the matrix have difficulty achieving the required uniform dispersion of CNTs for the formation of conductive pathways and face problems with the formation of agglomeration [29]. However, Rodriguez-Uicab et al. recently demonstrated the application of CNTs in aramid fiber reinforced polypropylene composites for in situ strain sensing where the composites were shown to be capable of sensing tensile strain during quasi-static and cyclic loading [17]. Composites with CNTs dispersed only in the thermoplastic matrix were compared with composites with CNTs both distributed along the fibers and dispersed in the matrix. Although the composites with CNTs along the fibers showed improved sensitivity, the method used to distribute CNTs along the fiber is designed for individual fibers which requires a separation of the Twaron fiber yarns and is thus not ideal for woven fabrics or large-scale production. Additionally, Ehlert et al. used self-assembled CNTs on aramid fibers for fiber strain sensors, however a single fiber rather than a laminate composite test specimen was used [30]. Thus, the current methods commonly used to add multifunctional properties to nonconductive fibers by introducing an integrated piezoresistive carbon element are insufficient for widespread use with aramid fiber reinforced composites.

Recently, Lin et al. demonstrated the creation of porous graphene films from the surface of commercial polymer materials using a $CO_2$ infrared laser [31]. The processing methodology and laser induced graphene (LIG) have since received increasing interest and have been investigated for a variety of applications due to the simplicity of the production process and the lack of necessary chemical modification to the material [32]. Among these applications is resistance-based strain sensing using the inherent piezoresistivity of the LIG surface [33–37]. For example, Rahimi et al. studied the use of highly flexible LIG-based strain sensors for sensing active motion of human subjects [34]. The LIG surfaces were transferred to polydimethylsiloxane (PDMS) which was then attached to a glove and shown to be capable of tracking strain effectively enough to determine the hand and finger position of the wearer. Additionally, Wang et al. demonstrated the use of freestanding LIG-based papers as embedded strain sensors within fiber-reinforced composites [36]. The LIG was fabricated as a buckypaper sensor which was embedded during the layup process and subsequently shown to be capable of tracking the strain of the host composite. However, although it has been demonstrated that LIG can be added to the surface of aramid [38–40], no research reported in the literature to this point has evaluated the use of piezoresistive LIG directly printed onto aramid fabrics for use in self-sensing of strain in fiber-reinforced composites.

This work fabricates and utilizes multifunctional aramid composites with integrated LIG for the self-sensing of strain and damage during mechanical loading of aramid fiber reinforced composites. To achieve this, aramid fabric is first coated with porous LIG using a $CO_2$ infrared laser. The resulting piezoresistive graphene surface covers the full surface area of the aramid fabric that is exposed to the laser, thus enabling sensing throughout the entire area of the composite. Notably, this laser treatment does not affect the specific strength of the fabric, thus the structural ability of the fabric remains intact [39]. Following the laser treatment, the fabric is laid up using traditional composite fabrication methods resulting in a sensing LIG layer within the composite. The composite samples are then loaded in a three-point bend testing configuration to establish the ability to track flexural strain. Additional samples are also tested using a tensile configuration to investigate the ability of the piezoresistive samples to detect both strain and damage due to tensile loads. The multifunctional composites are thus shown to be responsive to multiple types of applied loads similar to some of the loads that are typically experienced by aramid composites in service.

## 2. Experimental section

### 2.1. LIG process and composite fabrication

Aramid-based fiber reinforced composites with LIG were fabricated using common fabrication methods, and the aramid fabric received no treatment or chemical modification prior to the generation of the graphene from the aramid surface. The as-received plain-weave aramid fabric (Kevlar® KM2+, style 790, scoured surface finish CS-800, 22 warp and fill count, warp and fill yarn Kevlar KM2+ 850 d, fiber diameter 12 μm received from BGF Industries) was first coated with graphene via a laser irradiation process using a 60 W $CO_2$ laser engraver (Epilog Zing 16) operating in raster mode. During the laser process, the surface fibers of the aramid fabric are converted to a porous graphene coating, which remains attached to the surface of the fabric as the aramid itself is used as the precursor for the LIG generation with no external graphene source. To ensure optimal mechanical performance of the aramid fiber reinforced composites [39], the LIG was generated on the aramid fabric at an output power of 20%, an impulse per unit area of 400 dots per inch (DPI), and laser raster speed of 1 $cm^2\ s^{-1}$. For sensitivity comparison, two sets of fabrics were prepared, one set with LIG on only one side, and a second set with LIG on both sides of the aramid fabric. The resulting graphene surfaces were then imaged using a field emission scanning electron microscope (FE-SEM). Additionally, Raman spectroscopy was performed on the LIG coated aramid fabric using a Renishaw inVia confocal Raman microscope with a 633 nm laser source.

Following the completion of the LIG process, three layers of LIG coated aramid were used as preforms and then infused with an epoxy resin consisting of Epon 862 resin (received from Hexion) and curing agent W (received from Hexion) at a ratio of 100:26.4 using a standard vacuum-assisted resin transfer molding (VARTM) process. The composite was then cured at 177 °C under 100 psi pressure for 3 h in a hot press. After the epoxy matrix was fully cured, the composite panels, with thickness between 0.85 and 0.9 mm, were cut to dimensions of ~11.2 mm in width and ~85 mm in length according to ASTM standard D7264 three-point bend testing however, additional length was added to each sample to allow for the attachment of wire leads for electrical measurements during testing. Similarly, composite panels were also cut to dimensions of ~12.5 mm in width and ~160 mm in length for tensile testing according to ASTM standard D3039. Fiberglass tabs were attached to the ends of the tensile test samples using high shear strength epoxy (Loctite® 9430™ Hysol®) as is recommended in the ASTM standard. Finally, the specimens were coated around their perimeter with silver paint, and 33 gauge copper wires were connected to each silver paint ring using a combination of silver paint and epoxy (Loctite® Epoxy Instant Mix™ 5 Minute). A schematic of the completed test specimen can be seen in Fig. 1a and Fig. 1b. The described process was completed for both single-sided LIG aramid as well as double-sided LIG

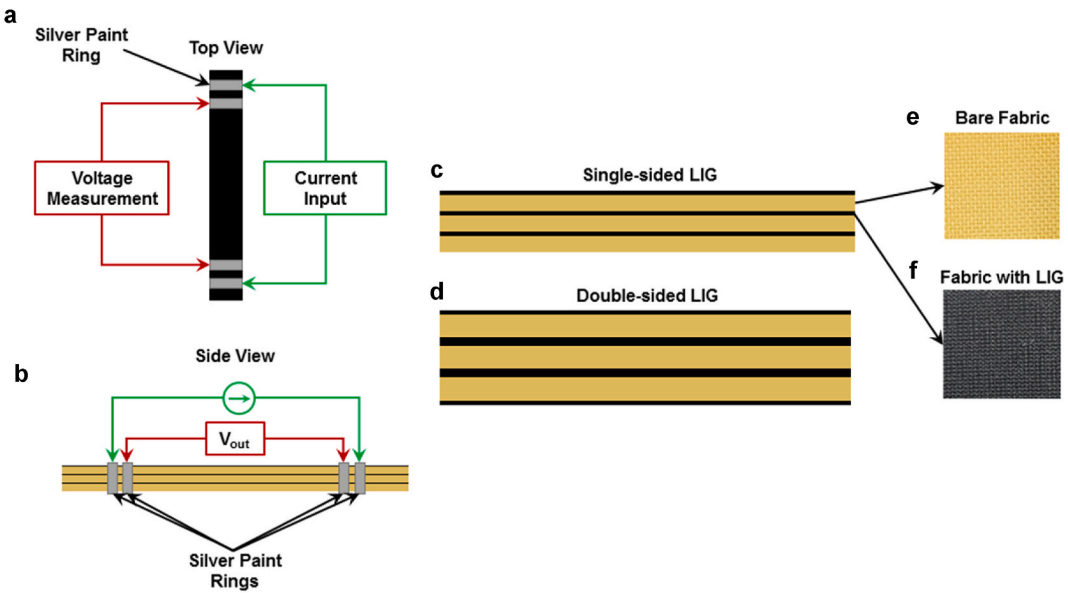


**Fig. 1.** (a) Schematic of sample tensile testing setup (front view), (b) schematic of sample testing setup (side view), (c) schematic of single-sided LIG aramid sample layup, (d) schematic of double-sided LIG aramid layup, (e) image of untreated aramid fabric, and (f) image of aramid fabric coated with LIG.

aramid as is shown in Fig. 1c and d respectively.

### 2.2. Mechanical testing

The ability of the LIG-coated aramid samples to sense tensile strain was evaluated by testing the LIG-coated aramid specimens in a tensile testing configuration per ASTM standard D3039. A minimum of five samples for both single sided and double sided LIG coated aramid composites were tested with the plain weave oriented at 0° and 90° from the applied load. An Instron load frame (Model 5982) with a 100 kN load cell was used at a crosshead speed of 1 mm/min. Throughout the duration of the test, 4 mA of DC current was applied through the sample with a BK Precision® model 9130 triple output programmable DC power supply using the copper wires connected to the outermost silver paint rings. The resulting voltage across the innermost silver rings from the copper wires was then measured with a NI 4431 data acquisition system (DAQ), and Ohm's law was used to calculate the resistance. An image and schematic of the tensile test setup is shown in Fig. 2. In addition to loading the samples to failure, cyclic testing was also completed at relatively low applied loads to determine the repeatability and consistency of the samples in detecting low levels of strain. In this case, the applied load, resistance of the sample, and strain of the sample were measured throughout the duration of the tests. To accurately measure the strain of the sample without interfering with electronic measurements, a VISHAY® micro-measurements & SR-4 general purpose strain gauge (120 ± 0.3% Ω, 2.075 ± 0.5% gauge factor) was attached to the surface of each sample using cyanoacrylate adhesive. The strain gauge was connected to a Wheatstone bridge for which the input voltage was provided and the output was monitored using a Transducer Techniques TMO-2 signal conditioner. To accurately measure the resistance of the sample at low strain values, a second Wheatstone bridge with a millivolt amplifier (Omega™ model MN1400-4) was used for the cyclic loading tests. The voltage input for the second Wheatstone bridge was provided by a Hewlett Packard model 6217 A DC power supply.

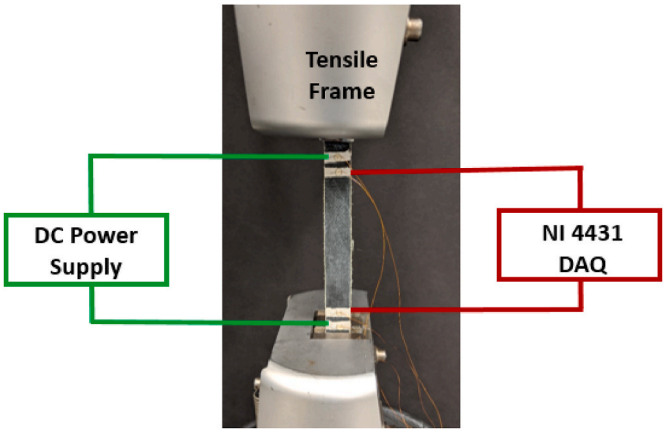


**Fig. 2.** Image and schematic of tensile test setup.

In addition to sensing tensile strain, the ability of the composites to sense flexural strain was evaluated by testing the prepared sample beams in a three-point bend configuration per ASTM standard D7264 with a span to thickness ratio of 20:1 to generate high strain levels. The same universal Instron load frame (Model 5982) and 100 kN load cell were used at a crosshead speed of 1 mm/min, and a minimum of five samples were tested. To eliminate current transfer from the sample to the load frame, non-conductive Kapton® tape was placed on the surface of the three-point bend pins. Throughout the duration of the test, 4 mA of DC current was again applied through the sample using the same DC power supply with the copper wires connected to the outermost silver paint rings. The resulting voltage across the innermost silver rings from the copper wires was then measured with the NI 4431 DAQ. The resistance of the sample during the test was calculated afterward using a standard four-point probe technique using the four silver paint rings and attached wires as the four probes. This methodology was completed for single-sided LIG aramid composites with the LIG at the top of the sample (under compression), single-sided LIG aramid composites with the LIG at the bottom of the sample (under tension), and double-sided LIG aramid composites. An image of the test setup can be seen in Fig. 3.

## 3. Results and discussion

### 3.1. LIG characterization

To evaluate the quality of the LIG coating on the surface of the aramid, characterization using SEM imaging was completed. In this case, a JEOL JSM-7800FLV field-emission SEM was used to image the surface of the fabric which can be seen in Fig. 4. Traditionally, the

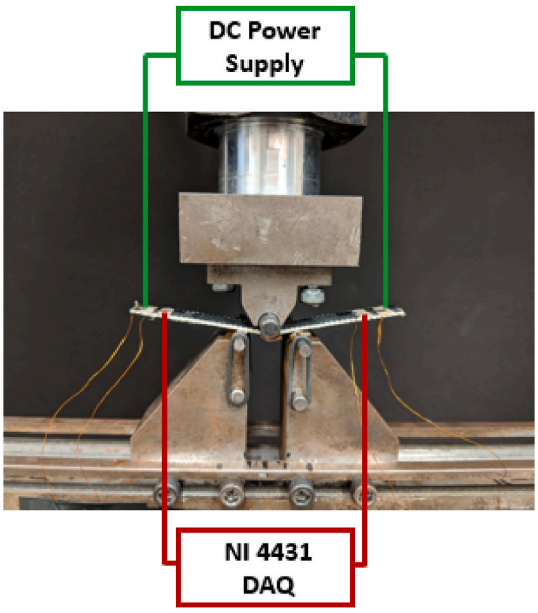


**Fig. 3.** Image of three-point bend test setup.

untreated aramid fabric surface consists of smooth, individual aramid fibers which lack the necessary roughness for a strong interfacial bond in a fiber reinforced polymer matrix composite (Fig. 4a, b, c). However, by subjecting the fabric to a defocused laser irradiation process, the high temperature poly (*p*-phenylene terephthalamide) (PPTA) is converted to amorphous carbon of various surface morphologies. This has been attributed to the photothermal effect and the breaking of the C═O and *N*–NC bonds within the aramid fabric resulting in the release of gaseous products and the conversion of the $sp^3$-carbon atoms to $sp^2$-carbon atoms leading to the formation of the porous graphitic interface [31,40]. It should be noted that this conversion only takes place on the surface fibers, and the remainder of the aramid fibers, which make up the majority of the weave, remain unaffected. The morphology and properties of the resulting carbon microstructure are dependent on the processing parameters such as the raster speed, raster density, and power. By generating the LIG at an operating power of 20%, the aramid surface exposed to the laser is covered with a fuzzy LIG morphology that is capable of providing mechanical reinforcement to the interlaminar region of the aramid composite (Fig. 4d, e, f, g, h, i) [39]. Further observation under SEM confirms that the LIG is comprised of a uniform layer of fuzzy microfibers which is approximately 10–15 μm in height. Following the VARTM process, this LIG layer was found to be approximately 6.5–7 μm thick in the one-sided configuration, which is below the diameter of a single Kevlar® filament, and 15 μm thick in the double sided configuration [39]. The morphology shown in Fig. 4d through Fig. 4i is an accurate representation of the layer covering the full surface area of the fabric that is exposed to the laser. For reference, Fig. 4l–m shown SEM images of the surface of a neat composite while Fig. 4n–o represent the surface of the LIG-treated composite. A comparison of the two sets of figures confirms a slightly increased surface roughness with the addition of the LIG interlayer. Due to the porosity of the interlayer, the LIG is fully infused with epoxy, however, a small fraction of LIG remains exposed at the surface of the composite. Although this results in a small increase in surface roughness, it also enables the direct connection between the LIG and the wire leads attached to the surface of the composite for electrical measurements. The resulting areal density of the single-sided LIG coated aramid fabrics is 0.0261 g/cm$^2$ while the areal density of the double-sided LIG coated aramid fabric is 0.0228 g/cm$^2$. For reference, the areal density of neat aramid fabric is 0.0281 g/cm$^2$. This density is decreased during the LIG process due to the conversion of the exposed fibers to porous LIG. It should be noted that the reported areal densities are that of LIG coated fabrics and not that of the individual LIG layer or of LIG coated composites with the supporting matrix. Rather, the weight of the fabric was measured using a high precision balance before and after the laser irradiation process. Given the reported low yield of the laser irradiation process (<5%), it is expected that the measured weight post-treatment is primarily that of the aramid fabric [38].

In addition, the LIG surface coating provides the originally electrically insulating aramid fabric with a piezoresistive layer. At a power of 20%, the aramid composite specimens with fabric coated on one side with LIG have a resistance value of 90–860 Ω for width between 11 and 14 mm and length between 85 and 110 mm. At the same laser power, the aramid composite specimens with fabric coated on both sides with LIG have an initial resistance between 60 and 120 Ω for width between 11 and 14 mm and length between 85 and 110 mm. It can be noted that the variations in resistance values are attributed to the need to manually adjust the defocusing distance of the laser. Additional analysis of the double-sided resistance values relative to the single-sided resistance values shows that adding the resistance of two equivalent single-sided samples in parallel results in a value that is similar to the values obtained from the double-sided sample. Thus, it can be inferred that each LIG surface on a single ply acts similarly to two resistors in parallel. It should be noted that the resistivity of the fabric can be further decreased by increasing the power of the laser or the raster pulsing density. However, the chosen parameters were used in order to generate a surface morphology capable of providing mechanical reinforcement to the composite and therefore taking advantage of the structural performance of the LIG [39]. It should be noted that the conductivity of the fabric was maintained throughout the VARTM process indicating that the LIG remained intact throughout the layup procedure. Therefore, the LIG coating provides the insulating aramid fabric with a multifunctional piezoresistive layer that, when monitored, is capable of providing information about the damage state of aramid fiber reinforced composites.

In addition to the qualitative analysis completed using SEM, Raman spectroscopy was also used to chemically characterize the LIG microstructure. The resulting spectra for both the untreated aramid fabric as well as the aramid fabric with LIG can be seen in Fig. 5. From Fig. 5a, the untreated aramid fabric has peaks at 1517 cm$^{-1}$, 1569 cm$^{-1}$, 1608.5 cm$^{-1}$, and 1647 cm$^{-1}$ all of which are characteristic of aramid fabric [38]. In contrast, Fig. 5b shows that the aramid fabric with LIG displays peaks at 1354 cm$^{-1}$, 1580 cm$^{-1}$, and 2699 cm$^{-1}$ which are representative of the D-band, G-band, and 2D-band of graphitic structures, respectively. The degree of aramid fabric surface graphitization can be evaluated by examining the ratio between the G- and D-bands. Pristine graphene shows no D-band peak, and instead shows a strong G-band peak [41]. With an increasing number of defects in the graphene or decreased distance between defects, the strength of the D-band peak relative to the G-band peak increases [41]. For reference, the LIG on polyimide film, which is the original substrate, was reported to have an $I_G/I_D$ ratio of 2.5 [31]. In contrast, the $I_G/I_D$ ratio of the LIG in this work is ~1.2, which indicates low graphene quality from the LIG on the surface of the fabric, however, the quality observed here is similar to that seen in previous analyses of LIG on aramid fabric [38–40]. Additionally, the added conductivity is sufficient for in situ resistance measurements and damage detection, while the maintaining the specific strength of the aramid fabric. Thus the resulting LIG is of sufficient quality for introducing multifunctionality into the aramid reinforcement.

### 3.2. Tensile testing

Throughout the duration of the tensile tests, the resistance of each sample was measured in situ using the four-point probe method, and the load was recorded by the Instron as can be seen in Fig. 6a. As the single-sided LIG aramid samples were loaded to failure, an increase in the electrical impedance of the sample was observed due to the inherent

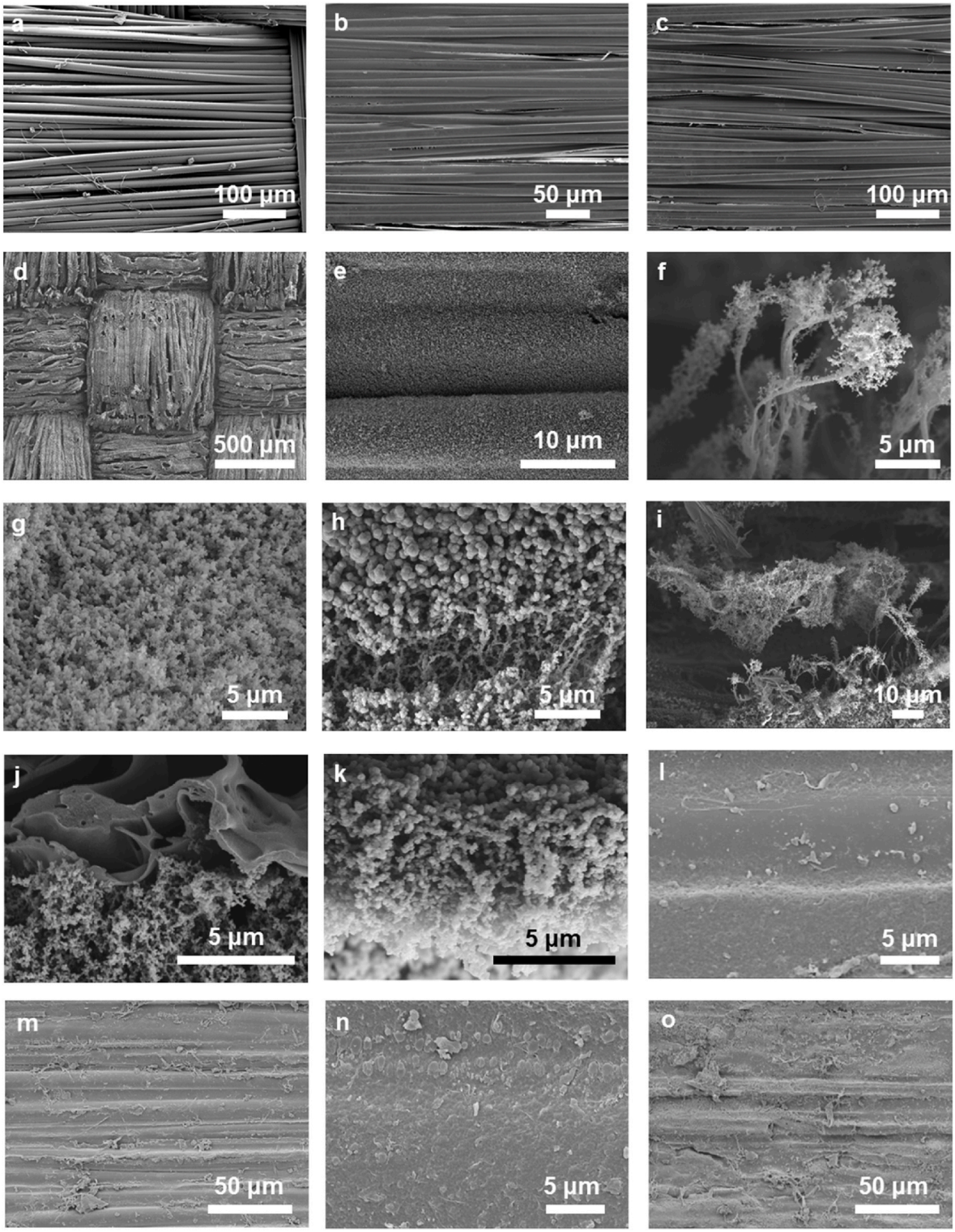


**Fig. 4.** (a–c) SEM images of the untreated aramid surface. (d–i) SEM images of LIG on aramid surface. (j–k) SEM images of LIG cross-section. (l–m) SEM images of neat aramid composite surface. (n–o) SEM images of LIG-treated aramid composite surface.

piezoresistivity of the sample. As tension is applied to the sample, the number of carbon-carbon contacts on each LIG surface is decreased which results in the observed increase in impedance. This effect is approximately linear during elastic deformation, and is thus predominantly dictated by the rate of extension. Beyond approximately ~3% increase in resistance correlating to ~25% of the final elongation, the resistance grows nonlinearly as the sample plastically deforms. During this region of tensile loading, irreversible separation between the LIG is observed. Additionally, as sudden damage occurs to the sample, either as delamination or as fiber breakage, the rate of increase in resistance changes due to a sudden separation of the conductive pathways on the LIG located on the surface fibers of each ply. This effect is particularly evident toward the latter portion of the test from. It should also be noted that the sudden drop in resistance observed at complete tensile failure of

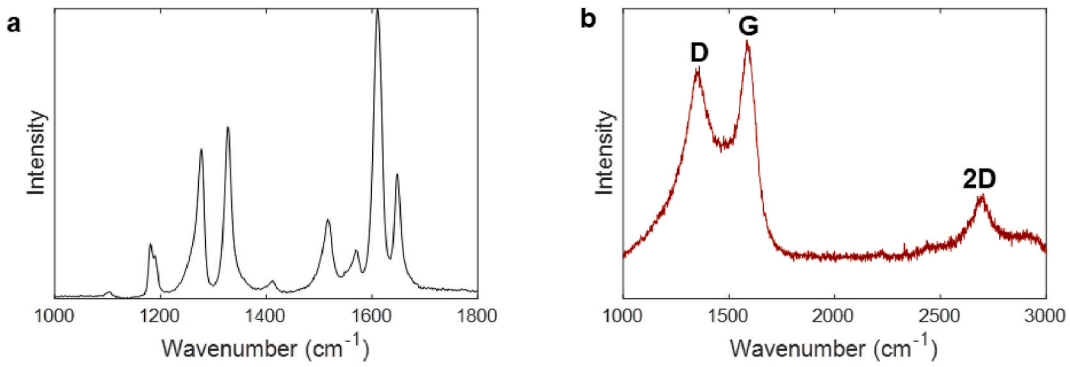


**Fig. 5.** Raman spectroscopy of (a) untreated aramid fabric and (b) aramid fabric coated with LIG.

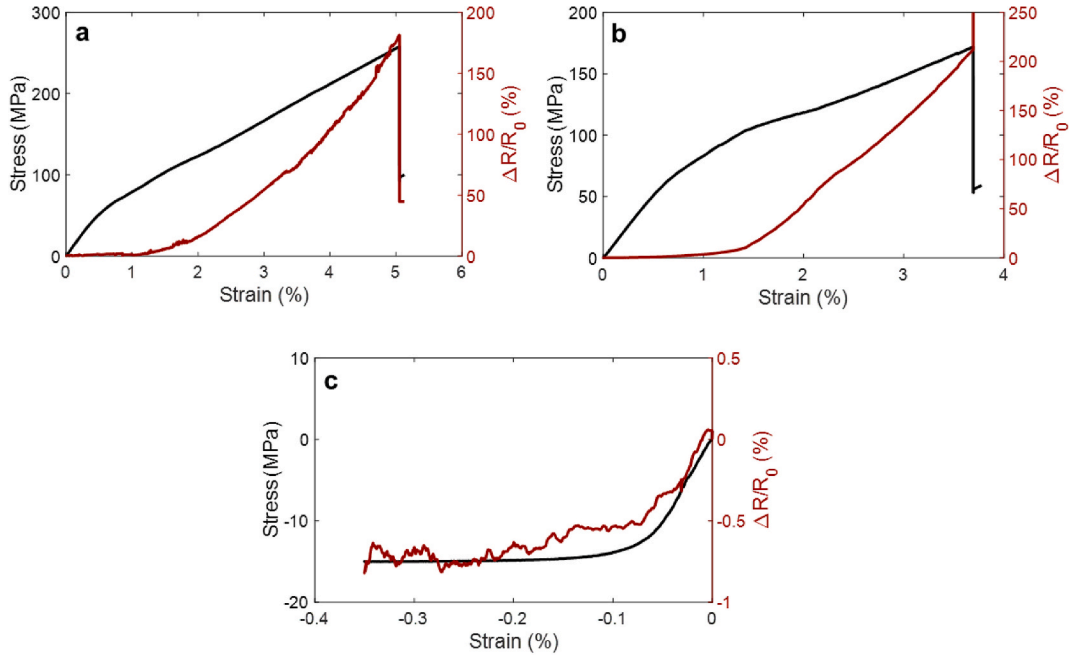


**Fig. 6.** Stress and percent change in resistance versus strain for (a) a single-sided LIG aramid sample under tension ($R_0$ = 323 Ω), (b) a double-sided LIG aramid sample under tension ($R_0$ = 86 Ω), and (c) a single-sided LIG aramid sample under compression ($R_0$ = 383 Ω).

the sample is due to the wire leads suddenly breaking off, and is not due to a change in the resistance of the sample. Similar to the single-sided LIG aramid samples, the double-sided samples also show an increasing trend in resistance with applied load and strain as can be seen in Fig. 6b. As before, there is a roughly linear increase during the first ~20% of the test which corresponds approximately to the elastic region of the material, after which, as the sample transitions to plastic deformation, the percent increase in resistance increases nonlinearly. Due to the higher graphene content and the decreased fiber volume resulting from the laser treatment process of the double-sided samples, fiber failure may be less likely to cause a sudden increase in resistance as was evident in the single-sided samples. As has been discussed previously, the exterior fibers in each tow, which are exposed to the laser, are irradiated and converted to piezoresistive LIG. As the sample is loaded, the interior fabric, not converted to LIG, decreases in cross-sectional area due to Poison's deformation, resulting in increased conductivity from the LIG coating. Therefore, as the fiber reinforcement begins to fail, there is little separation between the carbon contacts and the failure is thus not detectable via sudden increase in resistance in the double-sided LIG samples. It is interesting to note that although the double-sided LIG samples are more conductive than the single-sided samples, the maximum percent increase observed during tensile testing is similar to that seen from the single-sided samples which have a much higher initial resistance. It can also be observed from Fig. 6 that the double sided samples exhibit a decreased ultimate strength in comparison to the single-sided samples, and both sets of samples show a decrease relative to untreated aramid composites which possess an ultimate tensile strength of 331 ± 13 MPa. This is a result of the decreased density of the fabric due to the laser irradiation of the surface fibers. However, the areal density- or weight-specific strength of the fabric is maintained, and the interfacial strength is increased as investigated by Nasser et al. [39]. In addition to evaluating the piezoresistive response of the composite samples in tension, compression was also applied to single-sided samples for an improved understanding of the response of the LIG coating. Fig. 6c shows the applied stress and percent change in resistance versus the strain of the composite taken from compression to the point of buckling. The response indicates that compression of the sample results in increased conductivity which is a result of additional conductive contacts within the LIG. Therefore, the composites containing LIG are shown to sense both tension and compression through an increase or decrease in electrical impedance, respectively.

Although both sample sets demonstrated the ability to detect damage during tensile loading, it remains unclear from the obtained results whether the specimens are capable of repeatedly detecting low levels of

strain within the elastic region of the sample. Given the similar strain tracking behavior displayed by both sample sets when subjected to tensile loading, only the response of single-sided LIG coated aramid composites under repeated loading and unloading was investigated. Additionally, the single-sided samples have a higher maximum tensile load (although the specific strength is maintained for both sample sets [39]), therefore larger applied loads are possible prior to initiating significant damage within the sample. The samples were loaded and unloaded quasi-statically at a crosshead speed of 1 mm/min for several cycles between 0 MPa up to predetermined maximum stress levels of ~20, ~50, and ~100 MPa, and one precycle was allowed for stabilization. The maximum stress was varied between samples to determine repeatability of the sensing mechanism and to separate the strain and damage sensing capabilities. The resulting percent change in resistance and the strain of the sample versus time can be seen in Fig. 7a,c, e for the samples loaded to ~20, ~50, and ~100 MPa, respectively. To evaluate if plastic deformation or damage occurs within each cycle, the initial value of the stress, strain, and resistance are all considered. Changes in

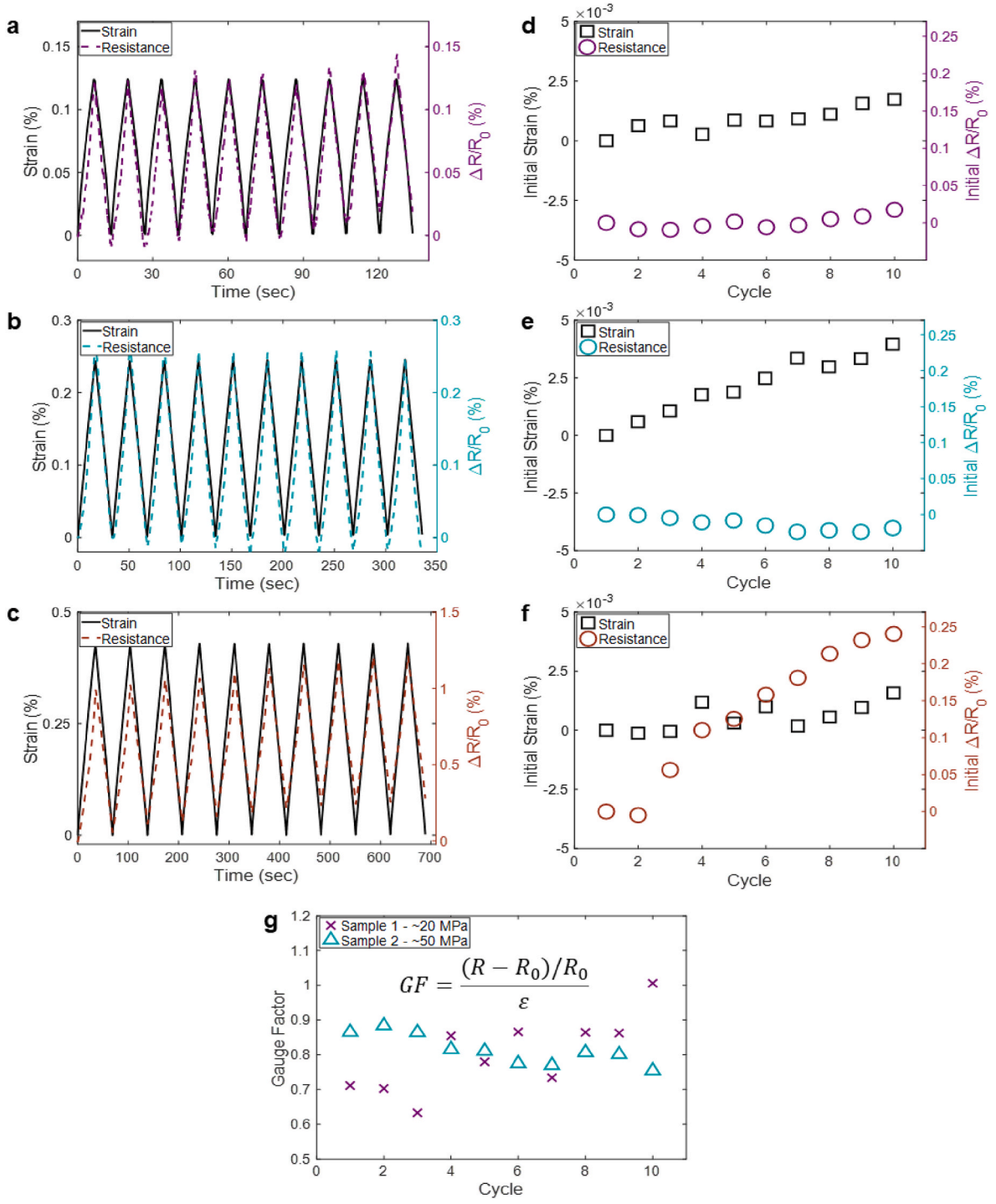


**Fig. 7.** (a) Percent strain and percent change in resistance, and (b) initial strain and resistance at the beginning of each cycle for a sample loaded cyclically to ~20 MPa with $R_0$ = 97 Ω. (c) Percent strain and percent change in resistance, and (d) initial strain and resistance at the beginning of each cycle for a sample loaded cyclically to ~50 MPa with $R_0$ = 92 Ω. (e) Percent strain and percent change in resistance, and (f) initial strain and resistance at the beginning of each cycle for a sample loaded cyclically to ~100 MPa with $R_0$ = 98 Ω. (g) Gauge factor versus cycle for two undamaged samples and gauge factor equation.

the trend between initial stress and strain indicate mechanical changes to the modulus of the composite which occur during the occurrence of plastic deformation or damage to the sample. At very low applied stress (~20 MPa), the initial strain remains relatively constant throughout the test, as shown in Fig. 7b. As the sample is unloaded and the stress approaches zero, the strain also returns to a value close to zero, indicating that no significant damage occurs within the sample as the composite is within the elastic regime. Throughout each cycle, the electrical impedance of the specimen follows the trend of the strain, thus the LIG is conclusively able to track the strain of the sample in the absence of damage. As the applied stress is increased to ~50 MPa (Fig. 7c–d), the initial strain begins to trend upward with increasing cycles. Since the sample is loaded and unloaded to the same stress values, the residual strain can be attributed to plastic deformation within the sample. The initial resistance, however, remains relatively constant, indicating that the damage is below the sensing threshold, until the stress is further increased to ~100 MPa. In Fig. 7e–f, the initial strain shows irregularity and a slight trend upward, which indicates that some plastic deformation and damage are occurring within the sample. Similarly, the initial resistance also shows an increasing trend with each cycle as the plastic deformation and damage are compounded. The observed increasing trend in residual resistance is similar to responses seen from composites containing CNTs when cyclically loaded [12,15,42], and is attributed to the irreversible separation between carbon-carbon contacts of the LIG on the aramid surfaces resulting from micro-damage during initial tensile loading and low-levels of plastic deformation in the aramid fabric. Therefore, from Fig. 7a and c, the samples are capable of repeatedly tracking low values in strain, while the increase in resistance after loading and unloading at higher loads, above a certain threshold (Fig. 7e), allows for retrospective detection of micro-damage due to the permanent increase in resistance from the initial measured value. The gauge factor of the first two samples was calculated for each cycle (Fig. 7g) according to the equation shown in Fig. 7g, where ε is the reading from the commercial strain gauge, R is the resistance of the composite, and $R_0$ is the initial resistance. The average gauge factor of Sample 3 was not considered since Sample 3 experienced damage and plastic deformation as was previously discussed. Thus, the average gauge factor of the undamaged samples is ~0.81, which is lower than the gauge factor of most commercial strain gauges. However, the integrated nature of the LIG used in this work overcomes this small decrease in gauge factor.

### 3.3. Three-point bend testing

An analysis of the load and resistance measurements taken during three-point bend testing of samples with different configurations provides insight into the strain sensing mechanism of the LIG coated aramid samples. The single-sided samples are inherently asymmetric in layup due to the added LIG layers, thus resulting in the majority of the LIG surfaces being either under compression or under tension during flexural loading depending on the orientation of the sample. Fig. 8 shows a schematic of the single-sided LIG coated aramid samples in both orientations during flexural loading and the associated midline. It should be noted that the LIG surfaces are separated by untreated Kevlar® fabric as only the exterior fibers of each tow are converted to LIG as discussed in Section 2.1. If the sample is oriented such that the LIG surfaces are facing upward during flexural loading (Fig. 8a), the majority of the sensing surfaces are under compression. In contrast, if the sample is oriented such that the LIG surfaces are facing downward during loading, the majority of the sensing surfaces are under tension (Fig. 8b). Thus, the two effects can be individually investigated during flexural loading by changing the orientation of the composite test specimen.

Fig. 9a shows the percent increase in resistance of a sample with the LIG surfaces oriented toward the bottom of the sample or primarily under tension. From the figure, when the majority of the LIG surfaces are experiencing positive strain, little to no linear increase is seen while the

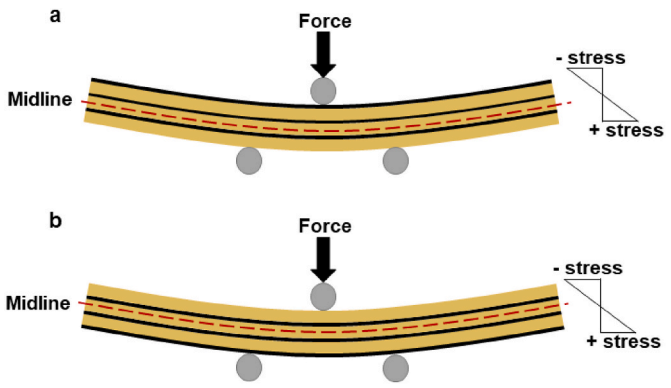


**Fig. 8.** (a) Schematic of single-sided LIG-coated aramid sample with LIG primarily under compression. (b) Schematic of single-sided LIG-coated aramid sample with LIG primarily under tension.

sample is elastically deformed (~10–15% of the final stress). This is likely due to the simultaneous separation between electrical carbon contacts on the intact LIG surfaces and the transverse compression of the LIG surfaces, which results in increased carbon-carbon contacts within the LIG microfiber bundles (Fig. 4d – i) and thus increased conductivity. As the sample continues to deform beyond the first 1%, accumulated damage and plastic deformation causes the resistance to increase nonlinearly as a result of drastically reduced conductive contacts on each LIG surface in tension. In the case of tension, the carbon-carbon contacts on each LIG surface are reduced or eliminated due to increased distance between each microstructure. In contrast, Fig. 9b shows the behavior of the sample when the majority of the LIG surfaces are primarily under compression. In the case of compression, the electrical impedance of the sample shows an initial decrease in resistance during the first ~40% of the test. This is attributed to both the compression of the LIG surfaces in the top half of the asymmetric composite which creates additional transverse contact between lamina, as well as additional carbon-carbon contacts on each LIG surface resulting in decreased electrical impedance. During the final 60% of the test, the response of the lamina in tension overtake the compressive effects, due to the large amount of separation between the LIG contacts, consequently resulting in increased electrical impedance with plastic deformation. However, the overall percent increase in resistance does not exceed 1.5% in contrast to the 6% increase observed from the previous configuration that was tension dominant.

For comparison, the applied load and resulting composite resistance versus crosshead extension of the double-sided LIG coated aramid composite is provided in Fig. 9c. In contrast to the single-sided LIG samples, the symmetric double-sided LIG samples show very small changes in resistance during flexural testing. This is due to the cancellation of the piezoresistive effects of the LIG while under compression and tension. Similar to the single-sided samples with LIG facing up (primarily under compression), the double-sided samples show some small initial decrease in impedance at the beginning of flexural loading. As previously discussed, transverse compression of the sample leads to increased contact and conductive pathways as a result of the compression of the LIG surfaces which results in increased conductivity. As the flexural strain increases, the tensile effects slightly overcome the compressive effects leading to an increase in impedance, however the response is not as significant as that seen from the single-sided samples. This may indicate that the increased conductivity of the double-sided samples and the functionality of the two LIG surfaces acting as resistors in parallel reduces the sensing capacity when a portion of the LIG surfaces are under tension. Effectively, the two results experienced separately by the single-sided LIG samples occur simultaneously in the double-sided samples due to the symmetry of the composite beam. Therefore, the outcome is a cancellation between increasing and

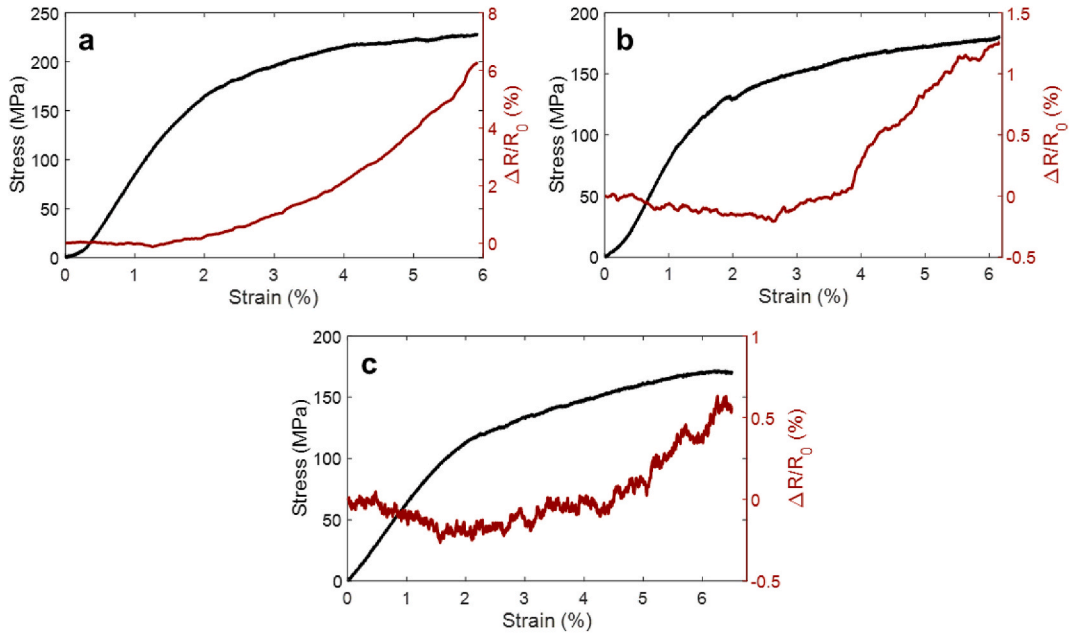


**Fig. 9.** Stress and percent change in resistance versus strain during three-point bend for (a) a single-sided LIG aramid sample with the LIG under tension ($R_0 = 700$ Ω), (b) a single-sided LIG aramid sample with the LIG under compression ($R_0 = 858$ Ω), and (c) a double-sided LIG aramid sample ($R_0 = 113$ Ω).

decreasing conductivity as is evidenced by the minimal changes observed in the measured resistance (less than 1% increase or decrease in resistance).

## 4. Conclusions

This work has exploited the piezoresistivity of LIG surfaces on aramid fiber reinforcement to fabricate a multifunctional composite with a fully integrated sensing component. The process used to achieve this is both low-cost and scalable which is promising for future applications and large-scale production. The microstructured LIG surfaces are directly printed onto woven aramid fabrics using a laser irradiation process after which the aramid fabric layers are combined via VARTM. The composite samples fabricated using single-sided and double-sided LIG coated aramid fabric were then shown to be piezoresistive and sensitive to both flexural and tensile loading. By measuring the resistance of the composite samples, changes in the state of the structures in the form of strain, plastic deformation, and damage are detectable both in situ by active measurements of the resistance, and retrospectively by permanent changes in the resistance of the test sample. As demonstrated during flexural loading of single-sided samples, both compression and tension of LIG aramid composites is detectable via a decrease and increase in impedance, respectively, as the microstructures comprising the LIG are pushed into contact or pulled apart. The samples with double-sided LIG coating were determined to be less sensitive to flexural loading due to a cancellation of these effects, yet proved equally capable of detecting high levels of tensile strain. When cyclically loaded, single-sided LIG aramid composites proved capable of detecting increasing strain at different rates as well as the ability to retrospectively detect loading via analysis of the residual resistance at maximum strain values below 1%. The result of this work is thus a promising multifunctional material with application in dynamic and unpredictable loading conditions where in situ tracking and damage detection is of benefit.

## CRediT authorship contribution statement

**LoriAnne Groo:** Conceptualization, Investigation, Writing - original draft. **Jalal Nasser:** Conceptualization, Investigation, Writing - review & editing. **Daniel Inman:** Project administration, Methodology, Writing - review & editing. **Henry Sodano:** Conceptualization, Project administration, Methodology, Funding acquisition, Supervision, Writing - review & editing.

## Declaration of competing interest

The authors declare that they have no known competing financial interests or personal relationships that could have appeared to influence the work reported in this paper.

## Acknowledgements

This work was supported by the National Science Foundation Graduate Research Fellowship Program under Grant # DGE 1256260 and the National Science Foundation under Grant # CMMI-1762369.

## Appendix A. Supplementary data

Supplementary data to this article can be found online at https://doi.org/10.1016/j.compscitech.2020.108541.

## References

[1] T.J. Singh, S. Samanta, Characterization of kevlar fiber and its composites: a review, Mater. Today: Proceedings 2 (4) (2015) 1381–1387.
[2] G. Zhou, L. Sim, Damage detection and assessment in fibre-reinforced composite structures with embedded fibre optic sensors-review, Smart Mater. Struct. 11 (6) (2002) 925.
[3] J. Leng, A. Asundi, Structural health monitoring of smart composite materials by using EFPI and FBG sensors, Sensor Actuator Phys. 103 (3) (2003) 330–340.
[4] S. Barré, M. Benzeggagh, On the use of acoustic emission to investigate damage mechanisms in glass-fibre-reinforced polypropylene, Compos. Sci. Technol. 52 (3) (1994) 369–376.
[5] V. Arumugam, C. Kumar, C. Santulli, F. Sarasini, A. Stanley, A global method for the identification of failure modes in fiberglass using acoustic emission, J. Test. Eval. 39 (5) (2011) 954–966.
[6] K. Schulte, C. Baron, Load and failure analyses of CFRP laminates by means of electrical resistivity measurements, Compos. Sci. Technol. 36 (1) (1989) 63–76.
[7] X. Wang, X. Fu, D.D.L. Chung, Strain sensing using carbon fiber, J. Mater. Res. 14 (3) (2011) 790–802.
[8] J.C. Abry, S. Bochard, A. Chateauminois, M. Salvia, G. Giraud, In situ detection of damage in CFRP laminates by electrical resistance measurements, Compos. Sci. Technol. 59 (6) (1999) 925–935.

[9] S. Wang, D.D.L. Chung, Self-sensing of flexural strain and damage in carbon fiber polymer-matrix composite by electrical resistance measurement, Carbon 44 (13) (2006) 2739–2751.
[10] S. Wang, D.D.L. Chung, J.H. Chung, Impact damage of carbon fiber polymer–matrix composites, studied by electrical resistance measurement, Compos. Appl. Sci. Manuf. 36 (12) (2005) 1707–1715.
[11] J. Wen, Z. Xia, F. Choy, Damage detection of carbon fiber reinforced polymer composites via electrical resistance measurement, Compos. B Eng. 42 (1) (2011) 77–86.
[12] L. Gao, E.T. Thostenson, Z. Zhang, T.-W. Chou, Sensing of damage mechanisms in fiber-reinforced composites under cyclic loading using carbon nanotubes, Adv. Funct. Mater. 19 (1) (2009) 123–130.
[13] S.-l. Gao, R.-C. Zhuang, J. Zhang, J.-W. Liu, E. Mäder, Glass fibers with carbon nanotube networks as multifunctional sensors, Adv. Funct. Mater. 20 (12) (2010) 1885–1893.
[14] E.T. Thostenson, T.-W. Chou, Carbon nanotube networks: sensing of distributed strain and damage for life prediction and self healing, Adv. Mater. 18 (21) (2006) 2837–2841.
[15] E.T. Thostenson, T.-W. Chou, Real-timein situsensing of damage evolution in advanced fiber composites using carbon nanotube networks, Nanotechnology 19 (21) (2008) 215713.
[16] L. Böger, M.H. Wichmann, L.O. Meyer, K. Schulte, Load and health monitoring in glass fibre reinforced composites with an electrically conductive nanocomposite epoxy matrix, Compos. Sci. Technol. 68 (7–8) (2008) 1886–1894.
[17] O. Rodríguez-Uicab, C. Martin-Barrera, A. May-Pat, A. Can-Ortiz, P.I. Gonzalez-Chi, F. Avilés, Electrical self-sensing of strain and damage of thermoplastic hierarchical composites subjected to monotonic and cyclic tensile loading, J. Intell. Mater. Syst. Struct. 30 (10) (2019) 1527–1537.
[18] H. Mahmood, L. Vanzetti, M. Bersani, A. Pegoretti, Mechanical properties and strain monitoring of glass-epoxy composites with graphene-coated fibers, Compos. Appl. Sci. Manuf. 107 (2018) 112–123.
[19] V.P. Veedu, A. Cao, X. Li, K. Ma, C. Soldano, S. Kar, P.M. Ajayan, M.N. Ghasemi-Nejhad, Multifunctional composites using reinforced laminae with carbon-nanotube forests, Nat. Mater. 5 (6) (2006) 457–462.
[20] Y. Zhou, F. Pervin, V.K. Rangari, S. Jeelani, Fabrication and evaluation of carbon nano fiber filled carbon/epoxy composite, Mater. Sci. Eng. 426 (1–2) (2006) 221–228.
[21] P.M. Ajayan, J. Suhr, N. Koratkar, Utilizing interfaces in carbon nanotube reinforced polymer composites for structural damping, J. Mater. Sci. 41 (23) (2006) 7824–7829.
[22] Z. Fan, M.H. Santare, S.G. Advani, Interlaminar shear strength of glass fiber reinforced epoxy composites enhanced with multi-walled carbon nanotubes, Compos. Appl. Sci. Manuf. 39 (3) (2008) 540–554.
[23] E. LaBarre, X. Calderon-Colon, M. Morris, J. Tiffany, E. Wetzel, A. Merkle, M. Trexler, Effect of a carbon nanotube coating on friction and impact performance of Kevlar, J. Mater. Sci. 50 (16) (2015) 5431–5442.
[24] L. Gao, T.-W. Chou, E.T. Thostenson, Z. Zhang, M. Coulaud, In situ sensing of impact damage in epoxy/glass fiber composites using percolating carbon nanotube networks, Carbon 49 (10) (2011) 3382–3385.
[25] Q. Zhang, J. Liu, R. Sager, L. Dai, J. Baur, Hierarchical composites of carbon nanotubes on carbon fiber: influence of growth condition on fiber tensile properties, Compos. Sci. Technol. 69 (5) (2009) 594–601.
[26] Q. An, A.N. Rider, E.T. Thostenson, Electrophoretic deposition of carbon nanotubes onto carbon-fiber fabric for production of carbon/epoxy composites with improved mechanical properties, Carbon 50 (11) (2012) 4130–4143.
[27] E. Bekyarova, E. Thostenson, A. Yu, H. Kim, J. Gao, J. Tang, H. Hahn, T.-W. Chou, M. Itkis, R. Haddon, Multiscale carbon nanotube– carbon fiber reinforcement for advanced epoxy composites, Langmuir 23 (7) (2007) 3970–3974.
[28] E.T. Thostenson, Z. Ren, T.-W. Chou, Advances in the science and technology of carbon nanotubes and their composites: a review, Compos. Sci. Technol. 61 (13) (2001) 1899–1912.
[29] F.H. Gojny, M.H.G. Wichmann, U. Köpke, B. Fiedler, K. Schulte, Carbon nanotube-reinforced epoxy-composites: enhanced stiffness and fracture toughness at low nanotube content, Compos. Sci. Technol. 64 (15) (2004) 2363–2371.
[30] G.J. Ehlert, H.A. Sodano, Fiber strain sensors from carbon nanotubes self-assembled on aramid fibers, J. Intell. Mater. Syst. Struct. 25 (17) (2014) 2117–2121.
[31] J. Lin, Z. Peng, Y. Liu, F. Ruiz-Zepeda, R. Ye, E.L. Samuel, M.J. Yacaman, B. I. Yakobson, J.M. Tour, Laser-induced porous graphene films from commercial polymers, Nat. Commun. 5 (2014) 5714.
[32] R. Ye, D.K. James, J.M. Tour, Laser-induced graphene: from discovery to translation, Adv. Mater. 31 (1) (2019) 1803621.
[33] L.-Q. Tao, H. Tian, Y. Liu, Z.-Y. Ju, Y. Pang, Y.-Q. Chen, D.-Y. Wang, X.-G. Tian, J.-C. Yan, N.-Q. Deng, An intelligent artificial throat with sound-sensing ability based on laser induced graphene, Nat. Commun. 8 (2017) 14579.
[34] R. Rahimi, M. Ochoa, W. Yu, B. Ziaie, Highly stretchable and sensitive unidirectional strain sensor via laser carbonization, ACS Appl. Mater. Interfaces 7 (8) (2015) 4463–4470.
[35] S. Luo, P.T. Hoang, T. Liu, Direct laser writing for creating porous graphitic structures and their use for flexible and highly sensitive sensor and sensor arrays, Carbon 96 (2016) 522–531.
[36] Y. Wang, Y. Wang, P. Zhang, F. Liu, S. Luo, Laser-induced freestanding graphene papers: a new route of scalable fabrication with tunable morphologies and properties for multifunctional devices and structures, Small 14 (36) (2018) 1802350.
[37] A. Chhetry, M. Sharifuzzaman, H. Yoon, S. Sharma, X. Xuan, J.Y. Park, MoS2-Decorated laser-induced graphene for a highly sensitive, hysteresis-free, and reliable piezoresistive strain sensor, ACS Appl. Mater. Interfaces 11 (25) (2019) 22531–22542.
[38] Y. Chyan, R. Ye, Y. Li, S.P. Singh, C.J. Arnusch, J.M. Tour, Laser-induced graphene by multiple lasing: toward electronics on cloth, paper, and food, ACS Nano 12 (3) (2018) 2176–2183.
[39] J. Nasser, L. Groo, L. Zhang, H. Sodano, Laser induced graphene fibers for multifunctional aramid fiber reinforced composite, Carbon 158 (2020) 146–156.
[40] H. Wang, H. Wang, Y. Wang, X. Su, C. Wang, M. Zhang, M. Jian, K. Xia, X. Liang, H. Lu, S. Li, Y. Zhang, Laser writing of janus graphene/kevlar textile for intelligent protective clothing, ACS Nano 14 (3) (2020) 3219–3226.
[41] R. beams, L.G. Cançado, L. Novotny, Raman characterization of defects and dopants in graphene, J. Phys. Condens. Matter 27 (8) (2015), 083002.
[42] L. Gao, E.T. Thostenson, Z. Zhang, T.-W. Chou, Coupled carbon nanotube network and acoustic emission monitoring for sensing of damage development in composites, Carbon 47 (5) (2009) 1381–1388.